2018

Changes in CO2 during the Ocean Anoxic Event 1d indicate similarities to other carbon cycle perturbations

Jon D. Richey
Texas State University-San Marcos

Garland R. Upchurch
Texas State University - San Marcos

Isabel P. Montanez
University of California, Davis

Barry H. Lomax
The University of Nottingham

Marina B. Suarez
The University of Texas at San Antonio

See next page for additional authors

Earth and Planetary Science Letters 491 (2018) 172–182

Contents lists available at ScienceDirect

Earth and Planetary Science Letters

www.elsevier.com/locate/epsl

Changes in CO_2 during Ocean Anoxic Event 1d indicate similarities to other carbon cycle perturbations

Jon D. Richey [a,*,1], Garland R. Upchurch [a], Isabel P. Montañez [b], Barry H. Lomax [c], Marina B. Suarez [d], Neil M.J. Crout [c], R.M. Joeckel [e], Greg A. Ludvigson [f], Jon J. Smith [f]

[a] Department of Biology, Texas State University, 601 University Dr., San Marcos, TX 78666, USA
[b] Department of Earth and Planetary Sciences, University of California, Davis, 1 Shields Ave., Davis, CA 95616, USA
[c] The School of Biosciences, Division of Agricultural and Environmental Sciences, The University of Nottingham, Sutton Bonington Campus, Sutton Bonington, Leicestershire, LE12 5RD, UK
[d] Department of Geological Sciences, The University of Texas at San Antonio, 1 UTSA Circle, San Antonio, TX 78249, USA
[e] Conservation and Survey Division, School of Natural Resources, Department of Earth and Atmospheric Sciences, and University of Nebraska State Museum, The University of Nebraska-Lincoln, 3310 Holdrege St., Lincoln, NE 68583-0996, USA
[f] Kansas Geological Survey, The University of Kansas, 1930 Constant Ave., Lawrence, KS 66047, USA

ARTICLE INFO

Article history:
Received 11 September 2017
Received in revised form 16 March 2018
Accepted 17 March 2018
Available online 5 April 2018
Editor: D. Vance

Keywords:
stomata
mid-Cretaceous pCO_2
Ocean Anoxic Event
carbon cycle perturbation
Lauraceae

ABSTRACT

Past greenhouse intervals of the Mesozoic were repeatedly punctuated by Ocean Anoxic Events (OAEs), major perturbations to the global carbon cycle and abrupt climate changes that may serve as relevant analogs for Earth's greenhouse gas-forced climate future. The key to better understanding these transient climate disruptions and possible CO_2-forced tipping-points resides in high-resolution, precise, and accurate estimates of atmospheric CO_2 for individual OAEs. Here we present a high-temporal resolution, multi-proxy pCO_2 reconstruction for the onset of mid-Cretaceous (Albian–Cenomanian Boundary) OAE1d. Coupling of pCO_2 estimates with carbon isotopic compositions ($\delta^{13}C$) of charcoal, vitrain, and cuticle from the Rose Creek Pit (RCP), Nebraska, reveals complex phasing, including a lag between the well-documented negative $\delta^{13}C$ excursion defining the onset of OAE1d and the CO_2 increase. This lag indicates that increased CO_2 or other C-based greenhouse gases may not have been the primary cause of the negative excursion. Our study reveals a pCO_2 increase within the interval of the negative $\delta^{13}C$ excursion, reaching a maximum of up to ~840 ppm (95% confidence interval −307 ppm/+167 ppm) toward its end. The reconstructed magnitude of CO_2 increase (~357 ppm) is similar to that of Late Cretaceous OAE2 but of smaller magnitude than that of other major carbon cycle perturbations of the Mesozoic assessed via stomatal methods (e.g., the Toarcian OAE [TOAE], Triassic–Jurassic boundary event, Cretaceous–Paleogene Boundary event). Furthermore, our results indicate a possible shared causal or developmental mechanism with OAE1a and the TOAE.

1. Introduction

Archives of the greenhouse climate system are punctuated by the sporadic occurrence of ocean anoxic events (OAEs) of regional to global extent (Schlanger and Jenkyns, 1976). OAEs were caused by increased organic preservation and/or productivity, leading to enhanced accumulation of marine organic matter as carbon-rich black shales (Jenkyns, 2010). The prevailing model for OAE initiation is CO_2-forced greenhouse warming due to volcanism (Barclay et al., 2010), methane hydrate release (Hesselbo et al., 2000), or thermogenic methane release (McElwain et al., 2005), coincident with changes in weathering and ocean circulation via feedbacks (Robinson et al., 2017). OAEs are further characterized by significant perturbations to the global carbon cycle recorded by ^{13}C-enrichment of the marine and atmospheric carbon reservoirs reflecting high rates of burial of ^{12}C-enriched organic carbon (Jenkyns, 2010). The positive C isotope excursions can be preceded by brief ^{12}C-enrichment of the marine and atmospheric carbon reservoir, providing a chemostratigraphic signature of these events. Because the change in the atmospheric carbon reservoir is transferred to the carbon isotopic composition of plants as they assimilate atmospheric CO_2, these events are recorded in the $\delta^{13}C$ of plants tissues and plant-dominated bulk

* Corresponding author.
E-mail address: jdrichey@ucdavis.edu (J.D. Richey).
[1] Current address: Department of Earth and Planetary Sciences, University of California, Davis, 1 Shields Ave., Davis, CA 95616, USA.

https://doi.org/10.1016/j.epsl.2018.03.035
0012-821X/

organic matter (Gröcke and Joeckel, 2008; Gröcke et al., 2006), allowing chemostratigraphic correlation to terrestrial sections that preserve individual OAEs. A potential complication to chemostratigraphic correlation is that the negative excursions can mask the OAE-defining positive excursion or themselves be masked by the positive excursion, which can lead to considerable variation in the isotopic expression of OAEs (Jenkyns, 2010). Because of these caveats, both stratigraphic and geochemical evidence is used to define and correlate OAEs.

OAE1d (the Breistroffer Event, ~100.5 Ma) was originally defined as a regional sub-OAE, but its occurrence in the Atlantic, Tethys, and Pacific oceans argues for its inclusion in the list of global OAEs (Robinson et al., 2008; Wilson and Norris, 2001). This perturbation to the carbon cycle is archived in the $\delta^{13}C$ records of planktonic foraminifera ($\delta^{13}C_{foram}$) (Wilson and Norris, 2001), bulk sediment/marine carbonate (Bornemann et al., 2017; Gambacorta et al., 2015; Petrizzo et al., 2008; Robinson et al., 2008), terrestrial bulk organics ($\delta^{13}C_{bulk}$), and fossil charcoal ($\delta^{13}C_{char}$) (Gröcke and Joeckel, 2008; Gröcke et al., 2006). Though considerable variability exists between $\delta^{13}C$ curves for OAE1d, most records document a long-term positive $\delta^{13}C$ excursion (~0.5–2‰) (Bornemann et al., 2017; Gambacorta et al., 2015; Petrizzo et al., 2008; Robinson et al., 2008; Wilson and Norris, 2001). Moreover, a few OAE1d $\delta^{13}C$ records reveal a short-term negative $\delta^{13}C$ excursion (~0.5–3‰) at the onset of OAE1d and preceding the longer-term positive excursion (Bornemann et al., 2017; Gröcke and Joeckel, 2008; Gröcke et al., 2006; Robinson et al., 2008; Wilson and Norris, 2001). This short-term negative $\delta^{13}C$ excursion has been interpreted as the release of ^{12}C-enriched carbon. Similar to other OAE events of the Mesozoic and early Cenozoic, the long-term positive excursion of OAE1d is interpreted to record increased marine productivity and enhanced organic matter burial in response to global warming and the collapse of upper water stratification (Wilson and Norris, 2001). In contrast, there are Tethyan sections that show no evidence of organic-rich sediments or the carbon isotope excursion that normally characterizes OAE1d (Luciani et al., 2004).

Reconstructions of atmospheric pCO_2 during Mesozoic OAEs (Barclay et al., 2010; McElwain et al., 2005; Naafs et al., 2016) have focused on OAE2 (~93 Ma), OAE1a (~120 Ma) and the Toarcian OAE (TOAE; ~183 Ma), with no estimates for OAE1d. Estimating pCO_2 during past carbon cycle perturbations is essential to refining our understanding of anthropogenic climate change. In particular, if the input of CO_2 into the system can be estimated at a high temporal resolution for OAEs for which independent estimates of global temperature are available, then such studies have the potential to constrain climate sensitivity (i.e. the temperature rise resulting from a doubling of CO_2).

A well-recognized approach to reconstructing paleoatmospheric CO_2 is the inverse relationship between stomatal density (SD) and index (SI) and atmospheric CO_2 (Woodward, 1987). These empirical methods have been used extensively to reconstruct CO_2 levels in the Cretaceous (see compilation in Li et al., 2014). Stomatal density, however, can be greatly affected by environmental factors related to leaf size because SD expresses stomatal frequency in terms of leaf area (Lomax and Fraser, 2015). SI mitigates this limitation given that it expresses stomatal frequency as a percentage of total leaf cells. Despite this, SI-based CO_2 estimates are associated with considerable uncertainties (10s to 100s ppm) because they rely on species-specific transfer functions inferred from nearest living relatives (McElwain et al., 2005).

Given the possibility of functional differences between modern and fossil plants and, thus, differences in response to changing pCO_2, estimates are considered more reliable if the targeted fossil species are calibrated to extant members of the same species (i.e. so-called "living fossils") (Lomax and Fraser, 2015). When this is not possible, estimates made using modern calibrations are considered "semi-quantitative". Recently, Franks et al. (2014) introduced a mechanistic model based on the universal leaf gas-exchange relationship and carbon isotopic discrimination in fossil species to reconstruct atmospheric CO_2. This approach is independent of closest living relatives and, thus, CO_2 estimates are arguably unaffected by species-specific responses to environmental conditions.

Here we develop a multi-proxy CO_2 time-series for OAE1d that presents pCO_2 estimates for the onset of the event of higher temporal resolution than previously published OAE records. We apply existing empirical-based transfer functions in order to evaluate different calibrations used to translate stomatal index into pCO_2 estimates (Barclay et al., 2010; Kürschner et al., 2008), as well as apply newly collected stomatal characteristics and fossil cuticle $\delta^{13}C$ values of *Pandemophyllum kvacekii* (Upchurch and Dilcher, 1990) to the recent mechanistic CO_2 model (Franks et al., 2014). We also use empirical estimates from three transfer functions to generate a consensus empirical pCO_2 curve and analyze all pCO_2 estimates (empirically- and mechanistically-derived) via LOESS analysis. The resulting consensus CO_2 record is compared to a newly integrated $\delta^{13}C$ curve developed using charcoal, vitrain, and cuticle and previously published $\delta^{13}C$ values from RCP (Gröcke and Joeckel, 2008; Gröcke et al., 2006). Correlation of the new terrestrial-based record to marine $\delta^{18}O$ and $\delta^{13}C$ time series for OAE1d (Wilson and Norris, 2001) is used to provide new insight into the relationship between CO_2, climate, and marine carbon perturbation during OAE1d.

2. Geologic setting and chronologic constraints

The study site, Rose Creek Pit (RCP; Fig. 1), is an inactive clay pit that exposes fluvial-estuarine sediments deposited on the eastern margin of the Western Interior Seaway (Gröcke and Joeckel, 2008; Gröcke et al., 2006). Palynological analysis indicates the presence of the Albian–Cenomanian boundary (ACB) at RCP by the recovery of definitive Upper Albian palynomorphs (*Disaltriangulisporites perplexus* and *Podocarpidites multesimus*) in the lower part of the section and Lower Cenomanian palynomorphs (*Foveogleicheniidites confossus* and *Artiopollis indivisus*) towards the top (Fig. 2; Gröcke et al., 2006). Gröcke et al. (2006) correlated the RCP $\delta^{13}C_{bulk}$ and $\delta^{13}C_{char}$ record to a marine $\delta^{13}C_{foram}$ time series developed for Ocean Drilling Project (ODP) site 1052, Blake Nose, western Atlantic Ocean (Wilson and Norris, 2001). Using downhole neutron porosity, the Blake Nose core was orbitally tuned, revealing ~19 and ~23 kyr precession cycle and a ~100 kyr eccentricity cycle signals, which they used to calculate a total duration for OAE1d of ~280 to 500 kyr (Gröcke et al., 2006; Wilson and Norris, 2001).

A ~0.5 to 3 million year (Myr) depositional hiatus occurs across the ACB at Rose Creek Pit, as indicated by the lack of the positive $\delta^{13}C$ excursion observed in the $\delta^{13}C_{foram}$ time series (Fig. 3a–b, Gröcke et al., 2006). The missing OAE1d positive $\delta^{13}C$ excursion is confirmed at other proximal localities (Fig. 3b, Gröcke and Joeckel, 2008). The unconformity has been correlated to the Dakota Formation D_2 sequence boundary, interpreted to record a global regression at the ACB (Koch and Brenner, 2009). Gröcke et al. (2006) hypothesize that the sea level low-stand during OAE1d inferred from the marine record correlates with a well-developed paleosol at RCP (Gröcke and Joeckel, 2008).

RCP preserves an abundant record of plant macrofossils and dispersed cuticle of Lauraceae and other vascular plant families. The systematic affinities of the RCP angiosperm leaf and cuticle flora are well-established by a combined study of its foliar architecture and cuticular anatomy (Upchurch and Dilcher, 1990), permitting leaf macrofossil species to be recognized from fragmented dispersed cuticle. Dispersed cuticle at RCP is preserved in many of

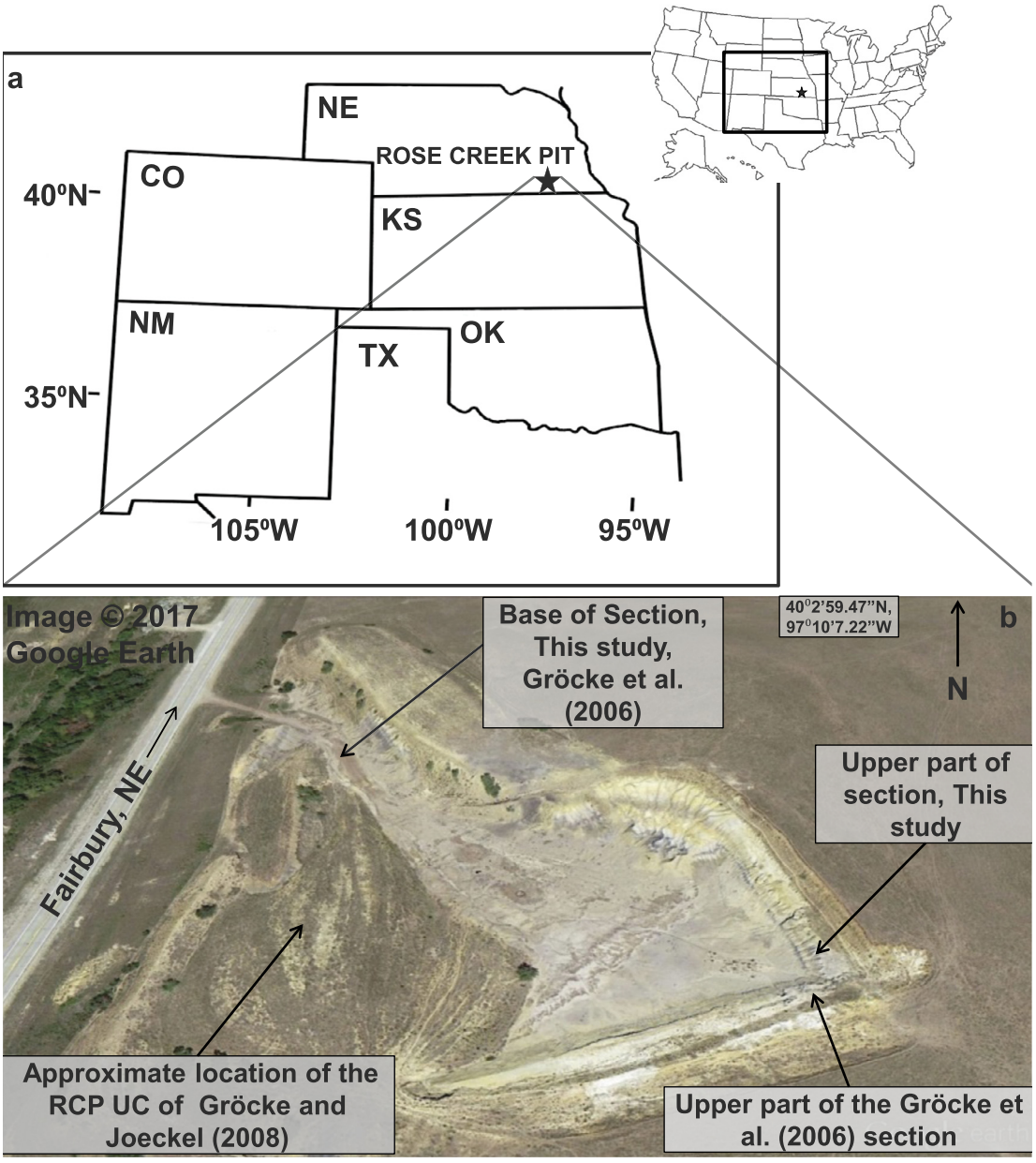

Fig. 1. Rose Creek Pit locality, S.E. Nebraska. **(a)** Map showing the location of the Rose Creek Pit. **(b)** Aerial image of the RCP locality, with locations of sampling labeled. GPS coordinates were recorded at the center of RCP.

the horizons of OAE1d, allowing us to evaluate changes in pCO_2 during that event.

3. Methods

3.1. Sampling

The RCP section was measured and bulk sediment samples were collected at 0.3 m intervals throughout ~9 m of exposed section (Figs. 1–2). Stratigraphically lower samples were collected from the same location in the pit as those of Gröcke et al. (2006), but due to weathering, samples above 4.5 m were collected from a laterally adjacent outcrop face. Because of this change in location (Fig. 1), the upper 2 m in this study shows some differences in facies thickness to the upper portion of the Gröcke et al. (2006) measured section (Fig. 2). Individual samples were restricted to a 2.5 cm thickness of sediment to provide a uniform sample thickness and minimize time-averaging of calculated CO_2 and $\delta^{13}C$ estimates. For each sample, ~0.3 to 1 kg of sediment was placed in 10% hydrochloric acid (HCl) overnight, rinsed until a neutral pH was obtained, and covered with a saturated solution of sodium pyrophosphate and −<10 ml of 30% hydrogen peroxide until fully disaggregated. Charcoal, vitrain, and cuticle were isolated by top sieving through a combination 500 and 90 µm mesh. All cuticle slides, bulk samples, and liquid-preserved residues are reposited at the Denver Museum of Nature and Science (DMNS locality 127).

3.2. Carbon isotope stratigraphy and analysis

Gymnosperm charcoal ($\delta^{13}C_{gym}$) and vitrain ($\delta^{13}C_{vit}$) (black, glassy, coalified plant material; Fig. 3c) were combined with previously published $\delta^{13}C_{char}$ and $\delta^{13}C_{bulk}$ measurements (Gröcke and Joeckel, 2008; Gröcke et al., 2006; Fig. 3b) to build an integrated organic carbon isotope ($\delta^{13}C_{org}$) time series for RCP (Fig. 3d). Salinity, which can influence the $\delta^{13}C$ signal of plants (Guy et al., 1980), is a particular concern at the RCP locality because of the

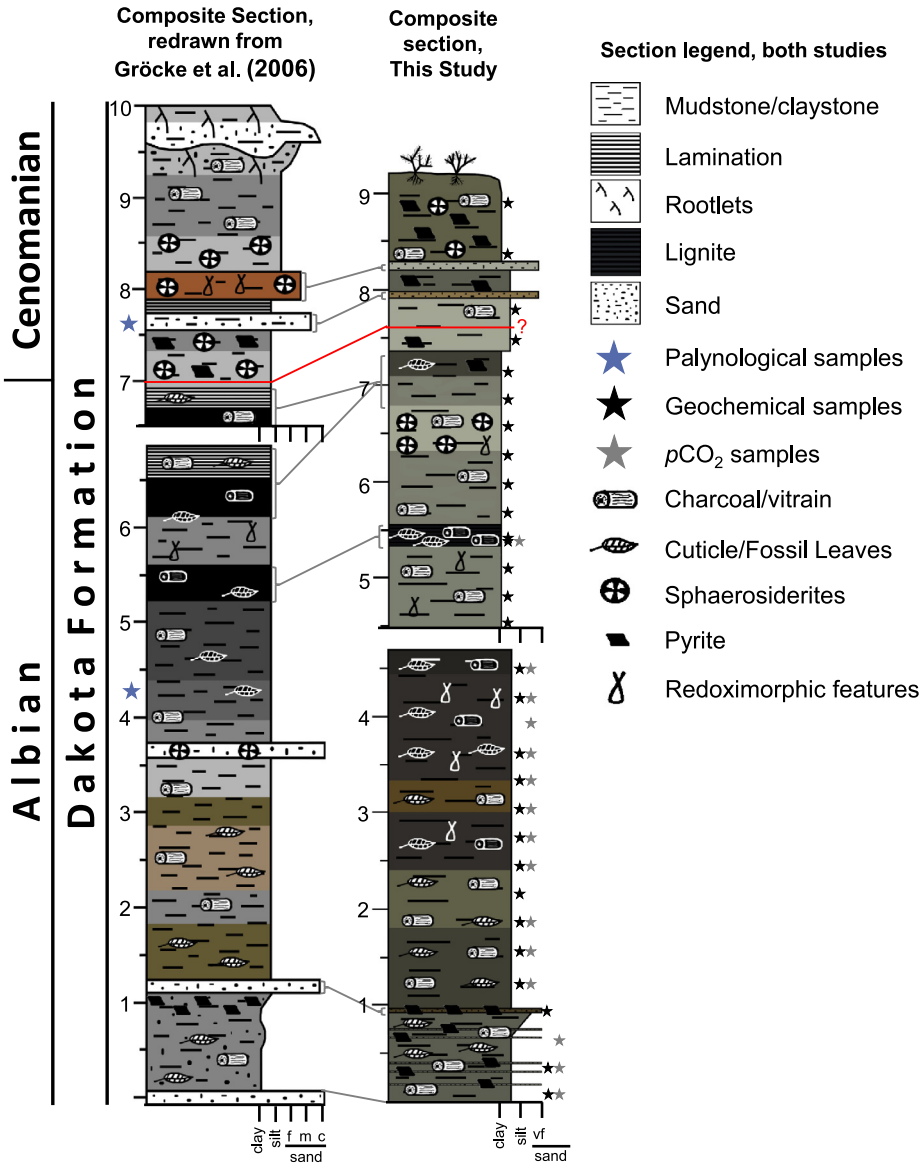

Fig. 2. Comparison of the section from Gröcke et al. (2006) and the composite section measured during this study. Gray brackets indicate stratigraphic features used to correlate between sections. Red line is inferred location of the Albian–Cenomanian Boundary in Gröcke et al. (2006). For the section from this study, the symbols are arranged to indicate the relative abundance of the features; stars indicate locations of geochemical (black) and cuticle samples (gray) for CO_2 reconstruction. (Please refer to the web version of this article to view more detailed colorized figure(s).)

documented marine influence (Retallack and Dilcher, 1981). Paleoecological analysis of RCP indicates that while angiosperms grew in and around the depositional environment and, therefore, dominate the leaf flora (Upchurch and Dilcher, 1990), gymnosperms inhabited higher ground such as levees and the dry floodplains of the hinterland (Retallack and Dilcher, 1981). Because of this, we elected to use gymnosperm charcoal exclusively for this study given that gymnosperm wood, and therefore charcoal, were not exposed to the possible high salinity environment of RCP during growth, negating the potential influence on its $\delta^{13}C$ signature.

Each charcoal sample was inspected under a stereomicroscope to separate gymnosperm and angiosperm charcoal. Sorting by type was not possible for vitrain because it does not preserve anatomy (Scott, 2010). The smallest fraction of gymnosperm charcoal and vitrain (~90 µm-sized fragments isolated via sieving) were concentrated and homogenized for analysis. This was done because it has been suggested that homogenized organic matter from a sufficiently large area (e.g. charcoal transported to the depositional environment of RCP, likely representing a watershed-sized area) represents a regional $\delta^{13}C$ signal, dampening local environmental effects (Ando and Kakegawa, 2007), and so that the signal would not be dominated by a single large charcoal fragment. Charcoal and vitrain samples were placed in 3M HCl to remove carbonates and heated to 60 °C to remove pyrite (Robinson and Hesselbo, 2004). $\delta^{13}C$ values were measured for isolated charcoal and vitrain at the University of Texas-San Antonio using a Costech Elemental Analyzer© coupled with a continuous-flow isotope ratio on a ThermoFinnigan Delta + XP mass spectrometer. External precision, based on repeated analysis of standards, is ±0.1‰. The resulting RCP isotopic curve was correlated with existing $\delta^{13}C$ records for RCP and nearby cores using stratigraphic position and correlation of distinct sedimentary markers (Fig. 2). In-line with earlier work, we have used the age model created by Wilson and Norris (2001) but adjusted all absolute ages to reflect the currently accepted age of the ACB of 100.5 Ma (Ogg et al., 2016).

Cuticle for isotopic analysis ($\delta^{13}C_{cut}$) was collected from the unmacerated cuticle that remained following stomatal analysis. Cuticle samples of the targeted species were rinsed in 3M HCl to

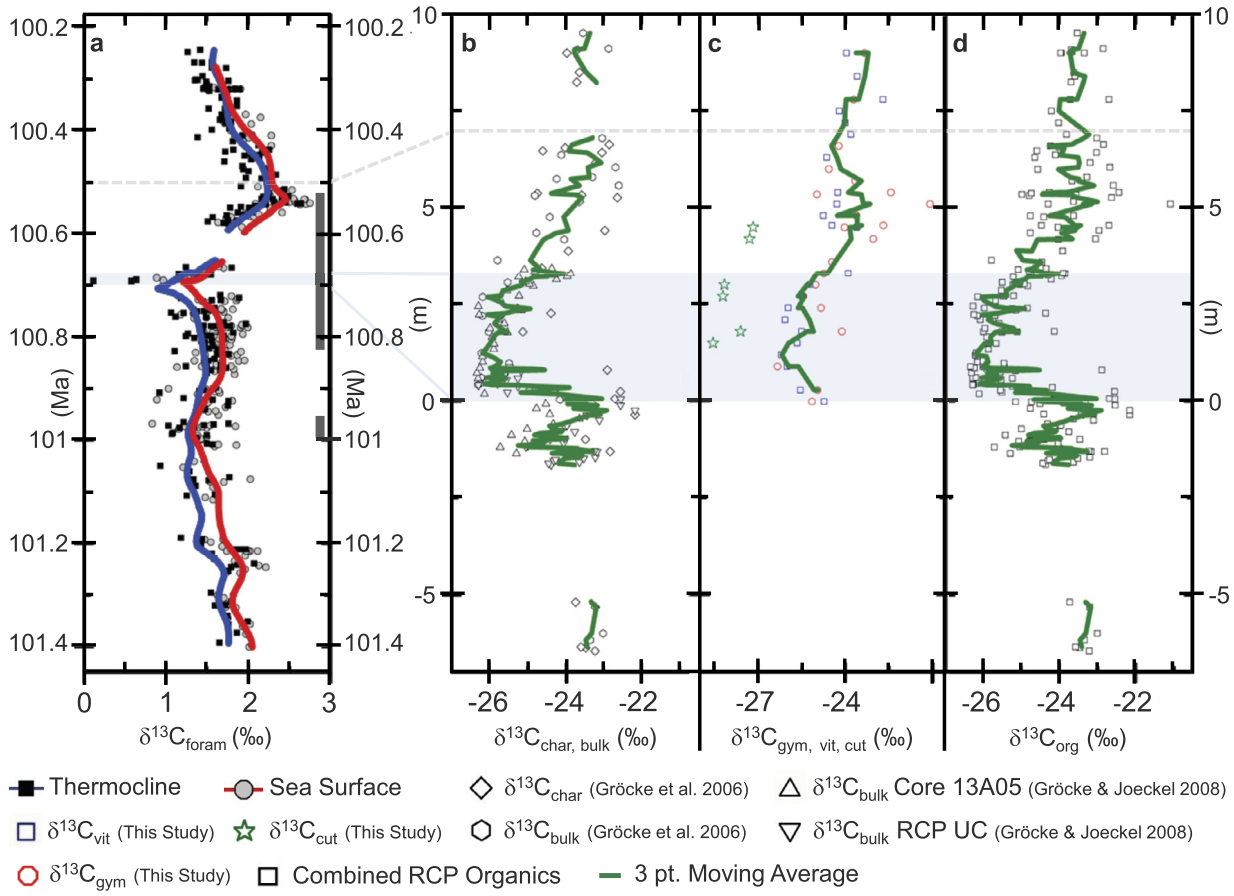

Fig. 3. Chemostratigraphy of this study and published studies (redrawn from Gröcke et al., 2006 and Gröcke and Joeckel, 2008) from RCP and nearby cores compared to published marine $\delta^{13}C$ time series (redrawn from Wilson and Norris, 2001). Blue shading indicates the negative $\delta^{13}C$ excursion of OAE1d. The gray dashed line is inferred location of the Albian–Cenomanian Boundary from Wilson and Norris (2001) and Gröcke et al. (2006). **(a)** $\delta^{13}C_{foram}$ from thermocline- (*Rotalipora* spp.) and sea surface-dwelling species (*Planomalina buxtorfi, Ticinella primula, Costellagerina lybica, Biticinella breggiensis*) isolated from ODP Site 1052, Blake Nose, western Atlantic. The black bar indicates the interval of laminated black shales; red and blue lines are 100 kyr to infinity trendlines (Wilson and Norris, 2001). **(b)** Published $\delta^{13}C$ of organic matter for RCP (Gröcke et al., 2006) and two proximal cores: one several m from RCP (Rose Creek Pit Upper Core [RCP UC]) and another from ~2.6 km SSW of RCP (Core 13A05) (Gröcke and Joeckel, 2008). **(c)** $\delta^{13}C$ of organic matter from this study. **(d)** Combined $\delta^{13}C$ data ($\delta^{13}C_{gym}$, $\delta^{13}C_{vit}$, $\delta^{13}C_{char}$, and $\delta^{13}C_{buk}$) for RCP and surrounding region.

remove carbonates and analyzed at the Stable Isotope Facility, University of California, Davis, using a PDZ Europa ANCA-GSL elemental analyzer interfaced to a PDZ Europa 20-20 IRMS to provide cuticle-specific $\delta^{13}C$ values for CO_2 modeling. External precision, based on repeated analysis of standards, is ±0.2‰. Two samples (SAM 1 and 4), did not yield enough cuticle for isotopic analysis. For those samples, $\delta^{13}C_{gym}$ and $\delta^{13}C_{vit}$ values were averaged and corrected for the average offset (−3.26‰) between $\delta^{13}C$ of cuticles and the $\delta^{13}C$ of gymnosperm charcoal and vitrinite at RCP; this value was used as a substitute for $\delta^{13}C_{cut}$. In addition, a large error (1‰) was used in the CO_2 model to account for the uncertainty in this approach.

3.3. Paleo-CO_2 reconstruction

Dispersed cuticle was macerated, when necessary, in various combinations of 10% chromium trioxide, household bleach, and/or sodium pyrophosphate prior to mounting for stomatal analysis. The target species for generating paleo-CO_2 estimates was *Pandemophyllum kvacekii*, an early member of the family Lauraceae (Upchurch and Dilcher, 1990). This species is common throughout the section, locally abundant (up to 25% of cuticle isolated from individual samples), and easy to identify (Upchurch and Dilcher, 1990). Cuticle was photographed and analyzed to calculate SI ($= S/[S+E] * 100$; where S is number of stomata and E is the number of epidermal cells including guard cells) and SD ($= S$/area [mm^2]). For SI, when possible, a target of 5000 counted cells was used, because this is the number of cells at which point variability in measurements stabilized. For each sample, an effort was made to isolate a single large cuticle fragment, such that 5000 cells could be counted from it, to completely minimize time-averaging of the pCO_2 signal. When this was not feasible, additional cuticles were measured until the 5000 cell quota was reached and the average of all *P. kvacekii* cuticles counted in each sampling interval was used.

Pandemophyllum kvacekii has a suite of specialized cuticular features found in Lauraceae, most notably brachyparacytic stomata with scale-shaped cuticular thickenings, and has venation comparable to that of the extant genera *Hypodaphnis* and *Eusideroxylon*, which have a basal position in molecular phylogenies of Lauraceae (Barclay et al., 2010; Chanderbali et al., 2001; Upchurch and Dilcher, 1990). Individual species within Lauraceae have been used to measure SI and estimate pCO_2 across the Cenomanian–Turonian Boundary (OAE2) (Barclay et al., 2010) and the Cretaceous–Paleogene Boundary (Steinthorsdottir et al., 2016), as well as for the Miocene (Kürschner et al., 2008).

Published empirical transfer functions derived from modern and fossil lauraceous species were used to estimate CO_2 concentrations from our SI data (Barclay et al., 2010; Kürschner et al., 2008). Kürschner et al. (2008) derived an equation to predict Miocene CO_2 by characterizing the stomatal response of herbarium specimens of *Laurus nobilis* and *Ocotea foetens* to modern changes in CO_2. Be-

cause their target species (extinct *Laurophyllum pseudoprinceps*) had no close modern equivalent, they cross-calibrated the stomatal response of that species with Miocene CO_2 levels inferred from three extant plant species, resulting in the following equation: $CO_2 = -46.011 * SI + 993.37$. No equation was derived to express error for the Kürschner et al. (2008) equation. Because of this, we calculate the error in estimates made using this method by inserting SI ±1 standard error of the mean into the equation.

Two additional transfer functions were defined by Barclay et al. (2010) using herbarium specimens of *Hypodaphnis zenkeri* and the *L. nobilis* data of Kürschner et al. (2008). For *L. nobilis*: $CO_2 = (-168.39 * Ln[SI]) + 790.93$ and for *H. zenkeri*: $CO_2 = (-27.447 * SI) + 559.67$. Barclay et al. (2010) derived separate ±95% confidence interval (CI) equations to estimate the error in the statistical relationship between SI and CO_2 for modern species. For *L. nobilis*: $-95\%\ CI = (-9.3347 * SI) + 467.28$ and $+95\%\ CI = (0.9177 * [SI]^2) - (42.578 * SI) + 777.21$. For *H. zenkeri*: $-95\%\ CI = (-10.279 * [SI]^2) + (132.43 * SI) - 64.375$ and $+95\%\ CI = (19.634) * [SI]^2) - (401.15 * SI) + 2341.8$.

As previously mentioned, a limitation of the SI method of pCO_2 reconstruction is the species-specificity of the stomatal response to pCO_2 and the need to use closely related modern equivalents. This is not possible with the extinct target species *P. kvacekii*. In order to combat the "semi-quantitative" nature of these estimates, we built a consensus CO_2 curve based on all empirical estimates.

To accomplish this, the CO_2 estimates obtained using the three transfer functions were resampled 10000 times from a distribution defined by the observed means and confidence intervals. The confidence intervals were skewed, especially for *H. zenkeri*, therefore a number of distributions were considered (including skew normal, gamma, and asymmetric Laplace, among others). Ultimately, an asymmetric double exponential distribution was used because it was found to give the best agreement between observed means and confidence intervals.

In addition, we assigned the individual curves qualitative statistical weights according to their position in the phylogeny of Lauraceae relative to that inferred for *Pandemophyllum* (Chanderbali et al., 2001). Extant species that nest well within the phylogeny of Lauraceae, high above the basal branches, were given the lowest weight because they are assumed to be the most anatomically and physiologically different from *Pandemophyllum*. Therefore, *L. nobilis* estimates were given the lowest statistical weight (0.15) because of that species' position high in the phylogeny of Lauraceae (Chanderbali et al., 2001). Conversely, modern species that occupy a basal position within the phylogeny of extant Lauraceae phylogeny were given the highest weight because they are assumed to be more anatomically and physiologically similar to *Pandemophyllum*. Thus, *H. zenkeri* estimates were given the greatest statistical weight (0.6) (Chanderbali et al., 2001). *L. pseudoprinceps* estimates were given an intermediate weight (0.25) because the transfer function is based on two modern genera of Lauraceae (*L. nobilis* and *O. foetens*) cross-calibrated with fossil genera and historical CO_2 concentrations (Kürschner et al., 2008). Even though the transfer function is based on two of the more derived species in the phylogeny of Lauraceae (Chanderbali et al., 2001), we think that the cross-calibration with historic CO_2 warrants its intermediate weighting.

More recently, Franks et al. (2014) introduced a mechanistic stomatal model for estimating paleo-CO_2 as an alternative to species-specific calibration curves. The model links the classic photosynthesis model (Farquhar et al., 1980) to anatomical and geochemical parameters that are readily recovered from the plant fossil record. Together, these parameters are used to derive estimates of plant performance due to optimization of plants to prevailing atmospheric CO_2. Stomatal size and number and the proportion of leaf area occupied by stomata are used to calculate maximum stomatal conductance ($g_{c(max)}$) to CO_2, and, thereby, operational stomatal conductance (taken as a fraction of $g_{c(max)}$). This is combined with the other components of conductance (leaf boundary layer and mesophyll conductance) to give total operational conductance to CO_2 diffusion from the atmosphere to the site of carboxylation. Cuticle $\delta^{13}C$ values are used as a proxy for leaf $\delta^{13}C$, given the negligible difference in their values from whole leaf tissue $\delta^{13}C$ for most species (Royer and Hren, 2017), in order to estimate c_i/c_a (the ratio of internal CO_2 to atmospheric CO_2) and, from this, determination of CO_2 drawdown and carbon fixation. These data are subsequently combined with the calculated assimilation rate (A_n) to estimate/calculate atmospheric CO_2 via the following equation: Atmospheric $CO_2 = A_n/(g_{c(tot)}[1 - c_i/c_a])$.

A sensitivity analysis of Franks et al. (2014) model by McElwain et al. (2016) indicates that the model is robust with respect to several important ecophysiological/environmental parameters, but is particularly sensitive to the prescribed photosynthetic rate (McElwain et al., 2016). We parameterized the mechanistic model using measured stomatal traits and cuticle $\delta^{13}C$ and a sensitivity analysis was carried out with a particular focus on A_0 (Tables s1 and s2). One set of CO_2 estimates was made using the prescribed A_0 (12) for woody angiosperms from Franks et al. (2014). A second set of CO_2 estimates was made following the methods outlined in McElwain et al. (2016). Using the vein density (D_v) of *P. kvacekii* (8.78; Feild et al., 2011), we utilize the equation that describes the relationship between D_v and g_{max} ($g_{max} = 27.574(D_v^2) - 93.365(D_v) + 512.84$) and the scaling relationship between g_{max} to theoretical maximum assimilation rate (tA_{max}) for *L. nobilis* ($tA_{max} = (4.25 \log_e(g_{max})) - 12.48$) (McElwain et al., 2015) to calculate a *P. kvacekii*-specific A_0 of 19.48. Most likely, this value represents an overestimation of A_0, but the use of the prescribed value (12) and the calculated value of 19.48 represents the range of possible values.

All stomata-based pCO_2 estimates were combined with those derived using the mechanistic model to generate a consensus pCO_2 curve using a locally weighted polynomial regression (LOESS) program (PAST freeware; https://folk.uio.no/ohammer/past/). For this analysis, a 0.1 smoothing parameter was used to access the temporal variability in pCO_2 estimates.

4. Results

4.1. Geochemistry

Temporal variability in $\delta^{13}C_{gym}$, $\delta^{13}C_{vit}$, and $\delta^{13}C_{cut}$ observed in this study are congruent with previously published $\delta^{13}C_{char}$ and $\delta^{13}C_{bulk}$ curves for RCP and the surrounding area (Gröcke and Joeckel, 2008; Gröcke et al., 2006) (Fig. 3b–c). Average pre-excursion $\delta^{13}C$ from $\delta^{13}C_{char}$ and $\delta^{13}C_{bulk}$ isolated across highway 15 from RCP (below −5 m; Fig. 1) is ∼−23.3‰ (Gröcke et al., 2006). Below the floor of the pit, $\delta^{13}C$ drops to ∼−25.2‰ (in the 3 pt. moving average) before rising back to the pre-excursion values seen below −5 m. Above the pit floor (0 m), the integrated $\delta^{13}C$ curve delineates a ∼3‰ negative excursion (∼3.0–3.3 m), reaching a $\delta^{13}C$ minimum of −26.3‰ at 1.2 m (Fig. 3d). The new integrated $\delta^{13}C$ record further confirms that the subsequent positive $\delta^{13}C$ excursion seen in most marine records for OAE1d (Bornemann et al., 2017; Petrizzo et al., 2008; Robinson et al., 2008; Wilson and Norris, 2001) is missing (Fig. 3d), as was previously documented for RCP (Gröcke and Joeckel, 2008; Gröcke et al., 2006). In this interval (above ∼3.3 m), $\delta^{13}C$ values return to pre-excursion values. For the remainder of the record, $\delta^{13}C$ values fluctuate around pre-excursion values.

Our analysis verifies the findings of previous paleoecological studies of RCP (Retallack and Dilcher, 1981; Upchurch and Dilcher,

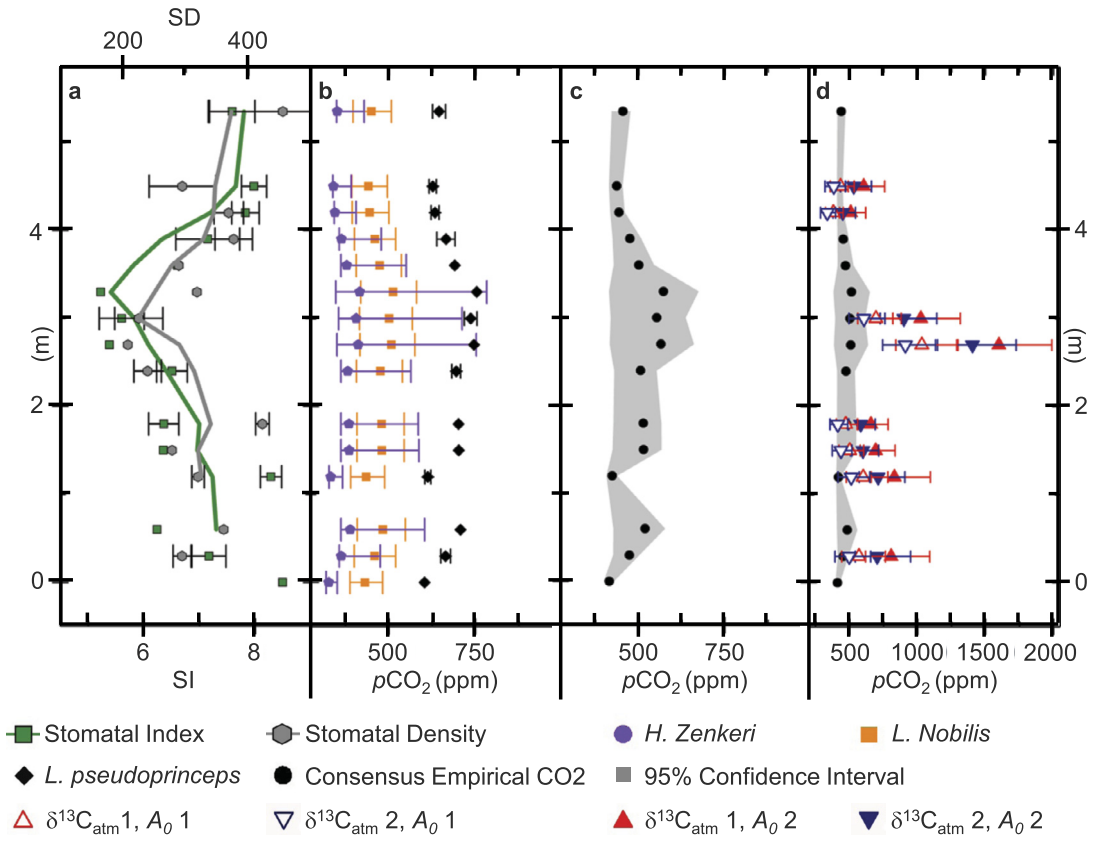

Fig. 4. Stomatal proxy pCO_2 calculated using fossil *Pandemophyllum kvacekii* from RCP. **(a)** Average stomatal index and stomatal density of all *Pandemophyllum kvacekii* cuticles counted in each sample. Error bars = 1 Standard Error of the Mean (SEM). Green and gray lines are 3-point moving averages. **(b)** pCO_2 estimates generated using SI in transfer functions derived using extant and fossil lauraceous species (see Methods). For *L. nobilis* and *H. zenkeri*, error bars = 95% confidence interval (CI) equations (Barclay et al., 2010). For *L. pseudoprinceps*, error bars = SI plus the standard error of the mean used in the *L. pseudoprinceps* equation (Kürschner et al., 2008). **(c)** Taxonomically-weighted consensus mean of SI-based CO_2 estimates (referred to as empirical; see Methods). Gray shaded area is calculated 95% CI for the taxonomically-weighted mean. **(d)** Mechanistic model-based (Franks et al., 2014) CO_2 estimates shown by color symbols and superimposed on taxonomically-weighted mean of empirical pCO_2 estimates. Note the change in pCO_2 scale. Error bars = 16th and 84th percentiles. $\delta^{13}C_{atm}$ values used are 1 = −7.36‰ and 2 = −8.41‰. A_0 1 = 12.00 and A_0 2 = 19.48 (see methods for justification of values).

1990) that gymnosperm charcoal dominates isolated charcoal from RCP, despite the fact that angiosperms dominate the leaf macrofossil and dispersed cuticle assemblages (Upchurch and Dilcher, 1990). It is probable that gymnosperm charcoal was transported to RCP by streams because charcoal floats, takes a great deal of time to waterlog, and has dispersal distances much greater than that of leaves (Scott, 2010). In addition, while angiosperm charcoal ($\delta^{13}C_{ang}$) mostly agrees with $\delta^{13}C_{gym}$ and $\delta^{13}C_{vit}$ where they co-occur, for two samples $\delta^{13}C_{ang}$ is ~1.6‰ more negative (SAM 1) and ~0.8‰ more positive (SAM 15) than the average of $\delta^{13}C_{gym}$ and $\delta^{13}C_{vit}$. While we cannot attribute this to any individual environmental factor, we take this increased variability in $\delta^{13}C_{ang}$ relative to $\delta^{13}C_{gym}$ and $\delta^{13}C_{vit}$ as confirmation that excluding $\delta^{13}C_{ang}$ from the integrated $\delta^{13}C$ curve is justified. Although we were able to isolate charcoal and vitrain throughout the measured RCP section, we were unable to recover cuticle above 5.35 m (with only one sample above 4.5 m, Fig. 4). Similarly, the sandstones that form the bottom of the pit are barren of dispersed cuticle. Thus, our CO_2 reconstruction is constrained temporally to the interval of the negative $\delta^{13}C$ excursion and the return to pre-excursion values, excluding the interval of the positive $\delta^{13}C$ excursion (Fig. 5c–d).

4.2. Empirical CO_2 estimates

Empirical CO_2 estimates based on stomatal transfer functions using extant or extinct lauraceous species show moderate variation, with most of the increase in CO_2 captured by the 95% confidence intervals (Fig. 4b). Estimates based on *L. nobilis* rise from 431 ppm (+51/−43 ppm) at 0 m to a high of 512 ppm (+67/−94 ppm) at 3.3 m (Fig. 4b; Table s2). Estimates based on *H. zenkeri* rise from 326 ppm (+25/−7 ppm) at 0 m to a high of 416 ppm (+365/−69 ppm) at 3.3 m (Fig. 4b; Table s2). Estimates based on *L. pseudoprinceps* rise from 602 ppm at 0 m to a high of 752 ppm at 3.3 m (Fig. 4b; Table s2). All the empirical CO_2 estimates follow the same general trend, rising slightly from 0 to 0.6 m, remaining relatively stable during the majority of the negative $\delta^{13}C$ excursion, then rising to a maximum between 2.7 to 3.3 m, before falling to concentrations that are slightly lower than pre-excursion values (Fig. 4a; Table s2).

The taxonomically weighted consensus curve, developed using the SI-based CO_2 estimates of all lauraceous species, is most closely aligned with results from the *L. nobilis* equation, even though *L. nobilis* nests high within the phylogeny of Lauraceae (Fig. 4c). That the consensus curve tracks most closely the *L. nobilis* estimates reflects the influence of the low estimates of CO_2 based on *H. zenkeri*, which has the effect of drawing down the consensus curve such that is tracks *L. nobilis*.

4.3. Mechanistic CO_2 estimates

Mechanistic estimates calculated here show a good deal of variation depending on the input parameters, as has been observed in previous studies (McElwain et al., 2016). Mechanistic estimates derived from different estimates of atmospheric $\delta^{13}C$ (from −7.31‰ to −8.41‰) vary by ~45 to 180 ppm, with the greater variation

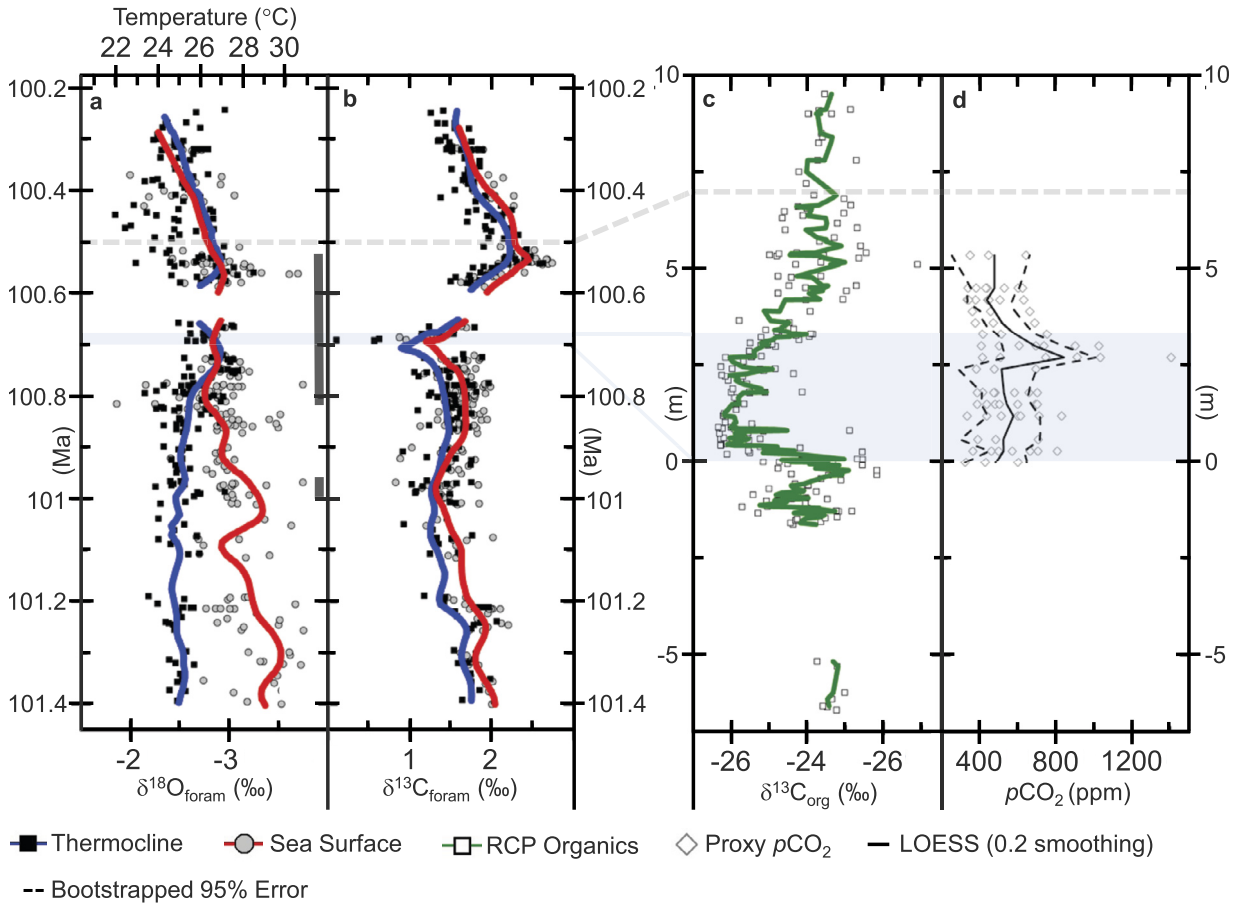

Fig. 5. Comparison of chemostratigraphy of RCP and nearby cores (Gröcke and Joeckel, 2008; Gröcke et al., 2006), LOESS consensus curve based on empirical and mechanistic CO_2 estimates, and published $\delta^{13}C$ and $\delta^{18}O$ time series (Wilson and Norris, 2001). The blue box indicates the negative excursion during OAE1d. The gray dashed line is the inferred location of the ACB in Gröcke et al. (2006) and Wilson and Norris (2001). **(a)** $\delta^{13}C_{foram}$ from thermocline dwelling species and sea surface dwelling species isolated from ODP Site 1052, Blake Nose, western Atlantic redrawn from Wilson and Norris (2001). **(b)** $\delta^{18}O_{foram}$ from thermocline dwelling species and sea surface dwelling species isolated from ODP Site 1052, Blake Nose, western Atlantic redrawn from Wilson and Norris (2001). Trendlines in a) and b) are 100 kyr to infinity fit. **(c)** Scatterplot of combined organic matter $\delta^{13}C$ ($\delta^{13}C_{gym}$, $\delta^{13}C_{vit}$, $\delta^{13}C_{char}$, and $\delta^{13}C_{bulk}$) from RCP and surrounding region. The green line is a 3 point moving average. **(d)** Combined empirical and mechanistic CO_2 estimates for *P. kvacekii*. The solid line is the locally weighted polynomial regression (LOESS) fit of the data (0.2 smoothing). Dashed lines are bootstrapped 2.5% and 97.5% errors.

seen at times of high pCO_2 (inferred from SI and SD). Raising the reference CO_2 assimilation rate (A_0), from the prescribed value of 12 to 19.48, derived in this study from vein density resulted in a variation of ~110 to 500 ppm with, the greatest variation seen at times of highest pCO_2. However, the use of both values of A_0 is justified because of the high vein density of *Pandemophyllum*, the range of A_0 values used encompasses higher values cited for related fossil Lauraceous species (up to 14; Franks et al., 2014), and the use of the higher value is intended to represent a range of possible values. Furthermore, for many of the estimates at inferred times of low CO_2, the empirical estimates are completely encompassed within the mechanistic estimates, implying that they are equally valid.

Temporally, the mechanistic CO_2 estimates follow the same trends of the empirical proxies, with significant overlap between mechanistic and empirical CO_2 estimates, especially at times at low CO_2 (Fig. 4d, Table s2). CO_2 estimates at 0 m range between 464 and 805 ppm, depending on input parameters, and rise at 2.7 m to a maximum CO_2 of 1032 to 1598 ppm. CO_2 subsequently falls to the lowest concentrations of the record (336–603 ppm). Notably, for the interval of highest CO_2 concentration estimated using the mechanistic model (2.7 m), the mechanistic estimates are substantially higher (by up to 1000 ppm) than the empirical based CO_2 estimates.

5. Discussion

5.1. Empirical vs. mechanistic estimates

If it is assumed that the mechanistic model is an improvement over taxon-specific stomatal-based empirical methods based on the aforementioned arguments, then our results are consistent with the previous finding that SI and SD saturate above ~700 ppm in angiosperms (Kürschner et al., 1996). However, an alternative explanation is that this saturation is due to problematic transfer functions that have not been calibrated for high CO_2 environments (and in particular, based on plants grown under elevated CO_2 in growth chambers). For example, using the *L. pseudoprinceps* equation of Kürschner et al. (2008) to estimate CO_2 from a hypothetical *P. kvacekii* fossil with an anomalously low and biologically implausible SI of 1 gives a max CO_2 of 947, consistent with CO_2 saturation at ~900 ppm or lower. Thus, we combine the empirical and mechanistic CO_2 estimates to define a consensus CO_2 curve (LOESS trend of Fig. 5d) that captures the same overall trend of a slight rise in pCO_2 coinciding with the most negative values in the integrated $\delta^{13}C$ curve, a slight drop in pCO_2 as $\delta^{13}C$ begins to increase at the onset of the positive $\delta^{13}C$ excursion, and, finally, a large increase in pCO_2 as $\delta^{13}C$ returns to pre-excursion values (Fig. 5c–d).

5.2. Comparison to other CO_2 estimates and paleoclimate indicators

The pattern of change in pCO_2 and the pre-CO_2 excursion background levels estimated in this study are consistent with several indicators of mid-Cretaceous paleoclimate and inferred atmospheric CO_2 levels. Retallack (2009), in his radiometrically-dated compilation of CO_2, temperature, and precipitation estimates from paleosols and cuticles collected in the southwestern United States, found that the generally dry and warm environment inferred from the Cedar Mountain Formation, Utah, was disrupted at ~99 Ma by a geologically brief instance of hot and humid climate with high precipitation attributed to OAE1d. Anomalous precipitation and temperature estimates were further attributed to rapid environmental change during OAE1d based on a leaf margin and area analysis of the Soap Creek Flora of the Cedar Mountain Formation (Arens and Harris, 2015). If the timing of the hypothesized rapid environmental change and the resulting anomalous precipitation and temperature estimates truly coincide with OAE1d, those results could be indicative of the rapid increase in pCO_2 during the OAE1d negative $\delta^{13}C$ excursion reconstructed in this study.

Recent compilations of mid-Cretaceous CO_2 estimates compare favorably with those generated in this study. Estimates from pedogenic carbonates indicate CO_2 levels between 352 and 1100 ppm around the ACB (Li et al., 2014; Ludvigson et al., 2015). Stomatal- and plant isotope-based estimates for the overall mid-Cretaceous interval suggest CO_2 concentrations ~2 to 5 times pre-industrial levels (i.e. 275 ppm) (Aucour et al., 2008; Haworth et al., 2005; Li et al., 2014; Passalia, 2009). Notably, a compilation of all published pCO_2 estimates for the ACB based on five different proxy methods (i.e. stomatal, pedogenic carbonate, liverwort and alkenone $\delta^{13}C$, and foraminiferal $\delta^{11}B$) and LOESS analysis of that data suggest a mean CO_2 concentration of 898 ppm (range 529–1351; Foster et al., 2017). Background, pre-CO_2 excursion levels presented here (440–575 ppm, Fig. 5d) and individual estimates calculated in this study (Table s2) fall well within the range of the aforementioned published CO_2 estimates (265–1351 ppm).

The reconstructed range in atmospheric CO_2 prior to and after the CO_2 spike at the end of the negative $\delta^{13}C$ excursion is less than the CO_2 threshold (~<800 ppm) for the initiation of Late Cretaceous Antarctic glaciation under conditions of cool summer orbit and high Antarctic elevation (Flögel et al., 2011), based on GENESIS version 3.0 with liquid cloud properties tuned to a modern anthropogenic atmosphere. This raises the possibility that the large sea level changes documented for OAE 1d and other intervals of the mid-Cretaceous (Koch and Brenner, 2009; Weissert and Lini, 1991) were glacioeustatic. The critical CO_2 concentration for the initiation of glaciation, however, may have been well below 800 ppm given the influence of paleogeography, paleotopography, and moisture source availability (Ladant and Donnadieu, 2016), potential for elevated levels of atmospheric methane (Beerling et al., 2011), and the uncertainty of the physical properties of pre-anthropogenic liquid clouds (Upchurch et al., 2015).

5.3. Comparison to attributes of other OAEs

The range over which CO_2 fluctuated during OAE1d reconstructed in this study (~357 ± 150 ppm, Fig. 5d) is comparable to that documented for the Late Cretaceous OAE2 (150–600 ppm) (Barclay et al., 2010), but smaller in magnitude than that estimated for other OAEs using the empirically derived SI method. These include the Cretaceous–Paleogene Boundary (up to 2000+ ppm; Beerling et al., 2002), TOAE (750–1750 ppm; McElwain et al., 2005), and Triassic–Jurassic Boundary (400–2000 ppm; Steinthorsdottir et al., 2011), though these estimates have yet to be reassessed using the mechanistic stomatal model. Moreover, estimated CO_2 inferred from compound-specific and bulk-rock $\delta^{13}C$ values indicate a change through OAE1a of 600 to 1400 ppm, although with considerable uncertainty (Naafs et al., 2016). The similar magnitude increase in CO_2 during OAE1d indicated by this study (from 483 ppm to 840 ppm; Fig. 5d) suggests an increase in radiative forcing of ~2.63 W/m^2 and an average global temperature increase of ~2.0 °C, assuming a global climate sensitivity of 0.8 °C for each W/m^2 forcing (Houghton et al., 2001; Rohling et al., 2012).

Our reconstructed pCO_2 record during OAE1d and inferred increase in radiative forcing suggest that OAE1d was an event on par with OAE2. This is notable because OAE2 is an unquestionably global event that caused a dramatic change in Earth system processes (Jenkyns, 2010). However, our calculated change in temperature (~2.0 °C) is well below the pronounced rapid temperature change estimated for OAE2 (~4 °C; Jenkyns, 2010) and additional evidence of temperature change during OAE1d is equivocal. An increase in sea surface and thermocline temperatures of ~1 °C at the beginning of the negative $\delta^{13}C$ excursion of OAE1d (Fig. 5a) is inferred from foraminiferal $\delta^{18}O$ time series (site 1052, Blake Nose, western Atlantic Ocean; Wilson and Norris, 2001), although subsequent analysis of the same data suggests a larger increase in temperature, coincident with the onset of the positive $\delta^{13}C$ excursion (Petrizzo et al., 2008). In addition, $\delta^{18}O$- and nannofossil-based sea-surface temperatures (SSTs) for OAE1d from the Vocontian Basin, France, indicate sea-surface warming at the end of the negative $\delta^{13}C$ excursion (Bornemann et al., 2005). While some $\delta^{18}O$ curves show negative shifts, possibly indicative of increased temperatures (Robinson et al., 2008), others show no change in $\delta^{18}O$, and therefore, inferred ocean temperatures, through the OAE1d interval (Bornemann et al., 2017; Gambacorta et al., 2015). These data, and the paucity of temperature estimates from outside the North Atlantic, make our estimates of temperature change challenging to evaluate.

Despite this, inferred changes in ocean temperature preceding OAE1d and other attributes of the event suggest similarities to other OAEs. Prior to the increase in temperatures associated with the onset of the negative $\delta^{13}C$ excursion, reconstructed SSTs in the western tropical Atlantic during the mid-Cretaceous (Wilson and Norris, 2001) suggest a long-term increase in thermocline temperatures and synchronous decrease in SSTs. These changes in temperature culminated in the breakdown of ocean stratification coincident with the onset of black shale deposition (Fig. 5a) suggesting that initiation of black shale deposition also preceded the onset of the subsequent positive $\delta^{13}C$ excursion. The temporal lag between the onset of black shale deposition and the peak of the positive $\delta^{13}C$ excursion, as well as cooling of the water column before OAE1d followed by warming of the deep ocean, is observed in other proximal OAE1d localities (Bornemann et al., 2005; Petrizzo et al., 2008).

The breakdown of water stratification during OAE1d is similar to that hypothesized for OAE1a, where changes in nannofossil abundance indicate a similar loss of stratification, possibly due to warming of intermediate waters (Erba, 2004; Wilson and Norris, 2001). In addition, both the early Toarcian OAE (TOAE; ~182 Ma) and OAE 1a (~120 Ma) are characterized by a pronounced, but brief negative $\delta^{13}C$ excursion followed by a more prolonged positive $\delta^{13}C$ excursion, which lags well behind black shale deposition (though, again, considerable variability exists between individual sections that preserve these events) (Erba et al., 1999; Hesselbo et al., 2000; Wilson and Norris, 2001). This is in contrast to the contemporaneity of black shale deposition and the positive $\delta^{13}C$ excursion for other OAEs (Robinson et al., 2017).

In addition to these previously noted similarities between OAE1d and the TOAE and OAE1a (Erba, 2004; Wilson and Norris, 2001), our work documents that the maximum rise in pCO_2 occurs well into the negative $\delta^{13}C$ excursion and that it postdates

the breakdown of ocean stratification and the onset of black shale deposition delineated by Wilson and Norris (2001) (Fig. 5). This out-of-phase relationship between change in CO_2 and geochemistry has been found in CO_2 reconstructions of both the TOAE (McElwain et al., 2005) and OAE1a (Naafs et al., 2016). This conclusion provides additional evidence of common causal and developmental mechanism underpinnings OAE1d, OAE1a, and the TOAE.

Both OAE1a and the TOAE have long been associated with volcanism in the form of large igneous provinces (LIPs). Likewise, OAE1d (~100.5 Ma) broadly coincides with the eruption of the central portion of the Kerguelen Plateau LIP (Site 1138; weighted mean age of 100.41 ± 0.71 Ma; Duncan, 2002). Analogous to OAE1a, the decrease in water column stability inferred from the convergence of surface- and intermediate-water foraminifera $\delta^{18}O$ values (Fig. 2a) could have been driven by warming of intermediate waters and a loss of water column stability with increased hydrothermal activity (Wilson and Norris, 2001). This conclusion, however, requires an unidentified mechanism to transport heat generated by the Kerguelen Plateau LIP to the north Atlantic. Although it is possible that widespread incorporation of continental crust into the Central Kerguelen Plateau was a source of ^{13}C-depleted carbon to the ocean and atmosphere and the source of the spike in CO_2 described in this study, there is little evidence for crustal contamination within the portion of the Kerguelen LIP that coincides with OAE1d (Frey et al., 2002). Given the aforementioned comparisons, we hypothesize that the similar characteristics shared between OAE1d and the TOAE and OAE1a suggest common causal and/or mechanistic linkages between the processes underpinning these events and that the common causal mechanism could be LIP volcanism.

6. Conclusions

The high temporal resolution and multi-proxy CO_2 reconstruction presented in this study represents the first CO_2 estimates generated for OAE1d. This CO_2 reconstruction elucidates the temporal relationship between atmospheric CO_2 and the carbon cycle perturbation across the onset of OAE1d and the Albian–Cenomanian boundary. Our findings indicate that the negative $\delta^{13}C$ excursion, which characterizes OAE1d, cannot be simply explained by changes in atmospheric CO_2. Moreover, the new estimates of background and maximum CO_2 during the negative $\delta^{13}C$ excursion, which characterizes the onset of OAE1d, are in broad agreement with other mid-Cretaceous CO_2 reconstructions and indicators of mid-Cretaceous paleoclimate. Our estimates also provide additional evidence of marked similarities in the development and behavior of OAE1d to OAE1a and TOAE and suggest a possible cause of LIP volcanism. Finally, this study further documents that the use of dispersed cuticle and improved stomatal based methods have the potential to provide high-resolution reconstructions of changes in atmospheric CO_2 during major Earth system perturbations.

Acknowledgements

We thank the DeBoer family for access to RCP. J.D.R was supported by National Science Foundation award EAR1148897 to IPM (University of California, Davis [UCD]), a National Science Foundation Graduate Research Fellowship under Grant #DGE-1144466 (Texas State University) and 1148897 (UCD), a Texas State University Thesis Research Support Fellowship, and a UCD Graduate Research Mentorship Fellowship.

Author contributions

G.R.U. and J.D.R. designed the study and collected the bulk sediment samples. R.M.J. coordinated fieldwork and assisted in the integration of the work presented here with prior results. R.M.J., J.J.S., and G.A.L. measured the stratigraphic section at RCP, which was corroborated by later work by J.D.R. J.D.R. processed samples, analyzed the data, and was the principal author of the manuscript. M.B.S. and I.P.M. provided facilities for the preparation of samples and carbon isotope analysis. G.R.U., M.B.S., I.P.M., and B.H.L. contributed to interpreting results and the writing and editing of the manuscript. N.M.J.C. provided help with statistical analysis. R.M.J., J.J.S., G.A.L., and N.M.J.C. provided comments and suggested edits to the manuscript.

Appendix A. Supplementary material

Supplementary material related to this article can be found online at https://doi.org/10.1016/j.epsl.2018.03.035.

References

Ando, A., Kakegawa, T., 2007. Carbon isotope records of terrestrial organic matter and occurrence of planktonic foraminifera from the Albian Stage of Hokkaido, Japan: ocean–atmosphere $\delta^{13}C$ trends and chronostratigraphic implications. Palaios 22, 417–432.

Arens, N.C., Harris, E.B., 2015. Paleoclimatic reconstruction for the Albian–Cenomanian transition based on a dominantly angiosperm flora from the Cedar Mountain Formation, Utah, USA. Cretac. Res. 53, 140–152.

Aucour, A.-M., Gomez, B., Sheppard, S.M.F., Thévenard, F., 2008. $\delta^{13}C$ and stomatal number variability in the Cretaceous conifer *Frenelopsis*. Palaeogeogr. Palaeoclimatol. Palaeoecol. 257, 462–473.

Barclay, R.S., McElwain, J.C., Sageman, B.B., 2010. Carbon sequestration activated by a volcanic CO_2 pulse during Ocean Anoxic Event 2. Nat. Geosci. 3, 205–208.

Beerling, D.J., Fox, A., Stevenson, D.S., Valdes, P.J., 2011. Enhanced chemistry-climate feedbacks in past greenhouse worlds. Proc. Natl. Acad. Sci. USA 108, 9770–9775.

Beerling, D.J., Lomax, B.H., Royer, D.L., Upchurch, G.R., Kump, L.R., 2002. An atmospheric pCO_2 reconstruction across the Cretaceous–Tertiary boundary from leaf megafossils. Proc. Natl. Acad. Sci. USA 99, 7836–7840.

Bornemann, A., Erbacher, J., Heldt, M., Kollaske, T., Wilmsen, M., Lübke, N., Huck, S., Vollmar, N.M., Wonik, T., 2017. The Albian–Cenomanian transition and Oceanic Anoxic Event 1d – an example from the boreal realm. Sedimentology 64, 44–65.

Bornemann, A., Pross, J., Reichelt, K., Herrle, J., Hemleben, C., Mutterlose, J., 2005. Reconstruction of short-term palaeoceanographic changes during the formation of the Late Albian 'Niveau Breistroffer' black shales (Oceanic Anoxic Event 1d, SE France). J. Geol. Soc. 162.

Chanderbali, A.S., van der Werff, H., Renner, S.S., 2001. Phylogeny and historical biogeography of Lauraceae: evidence from the chloroplast and nuclear genomes. Ann. Mo. Bot. Gard., 104–134.

Duncan, R.A., 2002. A time frame for construction of the Kerguelen Plateau and Broken Ridge. J. Petrol. 43, 1109–1119.

Erba, E., 2004. Calcareous nannofossils and Mesozoic oceanic anoxic events. Mar. Micropaleontol. 52, 85–106.

Erba, E., Channell, J.E.T., Claps, M., Jones, C., Larson, R., Opdyke, B., Silva, I.P., Riva, A., Salvini, G., Torricelli, S., 1999. Integrated stratigraphy of the Cismon Apticore (southern Alps, Italy): a "reference section" for the Barremian–Aptian interval at low latitudes. J. Foraminiferal Res. 29, 371–391.

Farquhar, G.D., von Caemmerer, S., Berry, J.A., 1980. A biochemical model of photosynthetic CO_2 assimilation in leaves of C_3 species. Planta 149, 78–90.

Feild, T.S., Brodribb, T.J., Iglesias, A., Chatelet, D.S., Baresch, A., Upchurch, G.R., Gomez, B., Mohr, B.A.R., Coiffard, C., Kvaček, J., Jaramillo, C.A., 2011. Fossil evidence for Cretaceous escalation in angiosperm leaf vein evolution. Proc. Natl. Acad. Sci. USA 108, 8363–8366.

Flögel, S., Wallmann, K., Kuhnt, W., 2011. Cool episodes in the Cretaceous — exploring the effects of physical forcings on Antarctic snow accumulation. Earth Planet. Sci. Lett. 307, 279–288.

Foster, G.L., Royer, D.L., Lunt, D.J., 2017. Future climate forcing potentially without precedent in the last 420 million years. Nat. Commun. 8, 14845.

Franks, P.J., Royer, D.L., Beerling, D.J., Van de Water, P.K., Cantrill, D.J., Barbour, M.M., Berry, J.A., 2014. New constraints on atmospheric CO_2 concentration for the Phanerozoic. Geophys. Res. Lett. 41, 4685–4694.

Frey, F.A., Weis, D., Borisova, A.Y., Xu, G., 2002. Involvement of continental crust in the formation of the Cretaceous Kerguelen plateau: new perspectives from ODP leg 120 sites. J. Petrol. 43, 1207–1239.

Gambacorta, G., Jenkyns, H.C., Russo, F., Tsikos, H., Wilson, P.A., Faucher, G., Erba, E., 2015. Carbon- and oxygen-isotope records of mid-Cretaceous Tethyan pelagic sequences from the Umbria–Marche and Belluno Basins (Italy). Newsl. Stratigr. 48, 299–323.

Gröcke, D.R., Joeckel, R.M., 2008. A stratigraphic test of the terrestrial carbon-isotope record of the latest Albian OAE from the Dakota Formation, Nebraska.

In: Joeckel, R.M., Ludvigson, G.A., Macfarlane, P.A. (Eds.), FIELD TRIP 2: Fluvial-Estuarine Deposition in the Mid-Cretaceous Dakota Formation, Kansas and Nebraska. Kansas Geologic Survey, Lawrence, KS, pp. 24–30.

Gröcke, D.R., Ludvigson, G.A., Witzke, B.J., Robinson, S.A., Joeckel, R.M., Ufnar, D.F., Ravn, R.L., 2006. Recognizing the Albian–Cenomanian (OAE1d) sequence boundary using plant carbon isotopes: Dakota Formation, Western Interior Basin, USA. Geology 34, 193–196.

Guy, R.D., Reid, D.M., Krouse, H.R., 1980. Shifts in carbon isotope ratios of two C_3 halophytes under natural and artificial conditions. Oecologia 44, 241–247.

Haworth, M., Hesselbo, S.P., McElwain, J.C., Robinson, S.A., Brunt, J.W., 2005. Mid-Cretaceous pCO_2 based on stomata of the extinct conifer *Pseudofrenelopsis* (Cheirolepidiaceae). Geology 33, 749–752.

Hesselbo, S.P., Gröcke, D.R., Jenkyns, H.C., Bjerrum, C.J., Farrimond, P., Morgans-Bell, H.S., Green, O.R., 2000. Massive dissociation of gas hydrate during a Jurassic oceanic anoxic event. Nature 406, 392–395.

Houghton, J.T., Ding, Y., Griggs, D.J., Noguer, M., van der Linden, P.J., Dai, X., Maskell, K., Johnson, C.A., 2001. Climate Change 2001: The Scientific Basis. Cambridge University Press, Cambridge, UK.

Jenkyns, H.C., 2010. Geochemistry of oceanic anoxic events. Geochem. Geophys. Geosyst. 11.

Koch, J.T., Brenner, R.L., 2009. Evidence for glacioeustatic control of large, rapid sea-level fluctuations during the Albian–Cenomanian: Dakota Formation, eastern margin of Western Interior Seaway, USA. Cretac. Res. 30, 411–423.

Kürschner, W.M., Kvaček, Z., Dilcher, D.L., 2008. The impact of Miocene atmospheric carbon dioxide fluctuations on climate and the evolution of terrestrial ecosystems. Proc. Natl. Acad. Sci. USA 105, 449–453.

Kürschner, W.M., van der Burgh, J., Visscher, H., Dilcher, D.L., 1996. Oak leaves as biosensors of late Neogene and early Pleistocene paleoatmospheric CO_2 concentrations. Mar. Micropaleontol. 27, 299–312.

Ladant, J.-B., Donnadieu, Y., 2016. Palaeogeographic regulation of glacial events during the Cretaceous supergreenhouse. Nat. Commun. 7, 12771.

Li, X., Jenkyns, H.C., Zhang, C., Wang, Y.I.N., Liu, L., Cao, K.E., 2014. Carbon isotope signatures of pedogenic carbonates from SE China: rapid atmospheric pCO_2 changes during middle–late early Cretaceous time. Geol. Mag. 151, 830–849.

Lomax, B.H., Fraser, W.T., 2015. Palaeoproxies: botanical monitors and recorders of atmospheric change. Palaeontology 58, 759–768.

Luciani, V., Cobianchi, M., Jenkyns, H.C., 2004. Albian high-resolution biostratigraphy and isotope stratigraphy: the Coppa della Nuvola pelagic succession of the Gargano Promontory (Southern Italy). Eclogae Geol. Helv. 97, 77–92.

Ludvigson, G.A., Joeckel, R.M., Murphy, L.R., Stockli, D.F., González, L.A., Suarez, C.A., Kirkland, J.I., Al-Suwaidi, A., 2015. The emerging terrestrial record of Aptian–Albian global change. Cretac. Res. 56, 1–24.

McElwain, J.C., Montañez, I.P., White, J.D., Wilson, J.P., Yiotis, C., 2016. Was atmospheric CO_2 capped at 1000 ppm over the past 300 million years? Palaeogeogr. Palaeoclimatol. Palaeoecol. 441, 653–658.

McElwain, J.C., Wade-Murphy, J., Hesselbo, S.P., 2005. Changes in carbon dioxide during an oceanic anoxic event linked to intrusion into Gondwana coals. Nature 435, 479–482.

McElwain, J.C., Yiotis, C., Lawson, T., 2015. Using modern plant trait relationships between observed and theoretical maximum stomatal conductance and vein density to examine patterns of plant macroevolution. New Phytol. 209, 94–103.

Naafs, B.D.A., Castro, J.M., De Gea, G.A., Quijano, M.L., Schmidt, D.N., Pancost, R.D., 2016. Gradual and sustained carbon dioxide release during Aptian Oceanic Anoxic Event 1a. Nat. Geosci. 9, 135–139.

Ogg, J.G., Ogg, G.M., Gradstein, F.M., 2016. 13 – Cretaceous. In: A Concise Geologic Time Scale. Elsevier, pp. 167–186.

Passalia, M.G., 2009. Cretaceous pCO_2 estimation from stomatal frequency analysis of gymnosperm leaves of Patagonia, Argentina. Palaeogeogr. Palaeoclimatol. Palaeoecol. 273, 17–24.

Petrizzo, M.R., Huber, B.T., Wilson, P.A., MacLeod, K.G., 2008. Late Albian paleoceanography of the western subtropical North Atlantic. Paleoceanography 23.

Retallack, G.J., 2009. Greenhouse crises of the past 300 million years. Geol. Soc. Am. Bull. 121, 1441–1455.

Retallack, G.J., Dilcher, D.L., 1981. Coastal hypothesis for the dispersal and rise to dominance of flowering plants. In: Niklas, K.J. (Ed.), Paleobotany, Paleoecology, and Evolution. Praeger, New York, pp. 27–77.

Robinson, S.A., Clarke, L.J., Nederbragt, A., Wood, I.G., 2008. Mid-Cretaceous oceanic anoxic events in the Pacific Ocean revealed by carbon-isotope stratigraphy of the Calera Limestone, California, USA. Geol. Soc. Am. Bull. 120, 1416–1426.

Robinson, S.A., Heimhofer, U., Hesselbo, S.P., Petrizzo, M.R., 2017. Mesozoic climates and oceans – a tribute to Hugh Jenkyns and Helmut Weissert. Sedimentology 64, 1–15.

Robinson, S.A., Hesselbo, S.P., 2004. Fossil-wood carbon-isotope stratigraphy of the non-marine Wealden Group (Lower Cretaceous, southern England). J. Geol. Soc. 161, 133–145.

Rohling, E.J., Sluijs, A., Dijkstra, H.A., Köhler, P., van de Wal, R.S.W., von der Heydt, A.S., Beerling, D.J., Berger, A., Bijl, P.K., Crucifix, M., DeConto, R., Drijfhout, S.S., Fedorov, A., Foster, G.L., Ganopolski, A., Hansen, J., Hönisch, B., Hooghiemstra, H., Huber, M., Huybers, P., Knutti, R., Lea, D.W., Lourens, L.J., Lunt, D., Masson-Demotte, V., Medina-Elizalde, M., Otto-Bliesner, B., Pagani, M., Pälike, H., Renssen, H., Royer, D.L., Siddall, M., Valdes, P., Zachos, J.C., Zeebe, R.E., 2012. Making sense of palaeoclimate sensitivity. Nature 491, 683–691.

Royer, D.L., Hren, M.T., 2017. Carbon isotopic fractionation between whole leaves and cuticle. Palaios 32, 199–205.

Schlanger, S.O., Jenkyns, H.C., 1976. Cretaceous Oceanic Anoxic Events: causes and consequences. Geol. Mijnb. 55, 179–184.

Scott, A.C., 2010. Charcoal recognition, taphonomy and uses in palaeoenvironmental analysis. Palaeogeogr. Palaeoclimatol. Palaeoecol. 291, 11–39.

Steinthorsdottir, M., Jeram, A.J., McElwain, J.C., 2011. Extremely elevated CO_2 concentrations at the Triassic/Jurassic boundary. Palaeogeogr. Palaeoclimatol. Palaeoecol. 308, 418–432.

Steinthorsdottir, M., Vajda, V., Pole, M., 2016. Global trends of pCO_2 across the Cretaceous–Paleogene boundary supported by the first Southern Hemisphere stomatal proxy-based pCO_2 reconstruction. Palaeogeogr. Palaeoclimatol. Palaeoecol. 464, 143–152.

Upchurch, G.R., Dilcher, D.L., 1990. Cenomanian Angiosperm Leaf Megafossils, Dakota Formation, Rose Creek Locality, Jefferson County, Southeastern Nebraska. United States Geological Survey Bulletin, pp. 1–55.

Upchurch, G.R., Kiehl, J.T., Shields, C.A., Scherer, J., Scotese, C., 2015. Latitudinal temperature gradients and high-latitude temperatures during the latest Cretaceous: congruence of geologic data and climate models. Geology 43, 683–686.

Weissert, H., Lini, A., 1991. Ice ages interludes during the time of Cretaceous greenhouse climate. In: Müller, D.W., MacKenzie, J.A., Weissert, H. (Eds.), Controversies in Modern Geology: Evolution of Geological Theories in Sedimentology, Earth History and Tectonics. Academic Press, London, pp. 173–191.

Wilson, P.A., Norris, R.D., 2001. Warm tropical ocean surface and global anoxia during the mid-Cretaceous period. Nature 412, 425–429.

Woodward, F.I., 1987. Stomatal numbers are sensitive to increases in CO_2 from preindustrial levels. Nature 327, 617–618.